

# Lattice expansion in ruthenium nanozymes improves catalytic activity and electro-responsiveness for boosting cancer therapy

Received: 30 November 2023

Accepted: 2 September 2024

Published online: 16 September 2024

 Check for updatesSongjing Zhong<sup>1,2</sup>, Zeyu Zhang<sup>1,3</sup>, Qinyu Zhao<sup>1,3</sup>, Zhaoyang Yue<sup>1,3</sup>, Cheng Xiong<sup>1,3</sup>, Genglin Chen<sup>1,2</sup>, Jie Wang<sup>1,2</sup> & Linlin Li<sup>1,2,3</sup> 

Nanozymes have been attracting widespread interest for the past decade, especially in the field of cancer therapy, due to their intrinsic catalytic activities, strong stability, and ease of synthesis. However, enhancing their catalytic activity in the tumor microenvironment (TME) remains a major challenge. Herein, we manipulate catalytic activities of Ru nanozymes via modulating lattice spacing in Ru nanocrystals supported on nitrogen-doped carbon support, to achieve improvement in multiple enzyme-like activities that can form cascade catalytic reactions to boost cancer cell killing. In addition, the lattice expansion in Ru nanocrystals improve the responsiveness of the nanozymes to self-powered electric field, achieving maximized cancer therapeutic outcome. Under the electrical stimulation provided by a human self-propelled triboelectric device, the Ru-based nanozyme (Ru1000) with a lattice expansion of 5.99% realizes optimal catalytic performance and cancer therapeutic outcome of breast cancer in female tumor-bearing mice. Through theoretical calculations, we uncover that the lattice expansion and electrical stimulation promote the catalytic reaction, simultaneously, by reducing the electron density and shifting the d-band center of Ru active sites. This work provides opportunities for improving the development of nanozymes.

Nanozymes, artificial nanomaterials with intrinsic enzyme-mimicking activities, have emerged as highly attractive and versatile class of nanomaterials in recent years<sup>1–4</sup>. Possessing the catalytic functions akin to natural enzymes, nanozymes offer distinct advantages, including high stability, controllable catalytic activity and facile synthesis<sup>4–6</sup>. They hold significant potentials for catalytic cancer therapy by utilizing specific molecules within tumors as substrates and generating toxic matters such as reactive oxygen species (ROS)<sup>7,8</sup>. However, it is still a challenging task to develop nanozymes that can efficiently catalyze the generation of large amounts of toxic ROS in the complex and changeable tumor microenvironment (TME) to achieve efficient killing of tumor cells. There is an urgent need to design and construct efficient nanocatalytic platforms with

adjustable activity, better responsiveness to the tumor micro-environment and high biocompatibility.

Both intrinsic structures and external stimulations using light, ultrasound and electricity influence the catalytic activities of nanozymes. The morphology and dimension<sup>9–12</sup>, element vacancy<sup>13–17</sup>, heteroatom<sup>8,18–22</sup>, surface chemistry<sup>23–26</sup> in nanozymes all influence their catalytic activities and substrate selectivities. From a geometric perspective, size and morphology often affect the exposed crystal planes and specific surface area of nanocatalyst, thereby influencing their catalytic activity<sup>11,27</sup>. From the perspective of electronic structure, the electronic energy levels of metal particles are also significantly changed due to the quantum size effect, which affects the orbital hybridization and charge transfer between the metal catalyst and the

<sup>1</sup>Beijing Institute of Nanoenergy and Nanosystems, Chinese Academy of Sciences, Beijing, China. <sup>2</sup>School of Nanoscience and Engineering University of Chinese Academy of Sciences, Beijing, China. <sup>3</sup>Center on Nanoenergy Research, School of Physical Science and Technology, Guangxi University, Nanning, China. ✉e-mail: [lilinlin@binn.cas.cn](mailto:lilinlin@binn.cas.cn)

substrate<sup>26,28,29</sup>. Moreover, doping of metal/non-metal atoms and vacancy engineering have also been utilized to modulate the catalytic activity of nanozymes by adjusting their surface electronic structure and energy band structure<sup>29–31</sup>. Precise and rational modulation of active site configurations is crucial for achieving nanozymes with distinct characteristics and high catalytic activity.

Besides optimizing intrinsic structure, noninvasive exogenous stimuli, including near-infrared light<sup>32–34</sup>, ultrasound<sup>13,35–37</sup>, magnetic<sup>38</sup> and electric fields<sup>39–41</sup>, have been applied to enhance the catalytic activity of nanozymes. Particularly, electric field as a clinically applied modality of cancer treatment has a deep and wide driving field that can cover the entire tumor tissue to avoid possible tumor recurrence<sup>42</sup>. Moreover, electrical stimulation can be exerted via a self-powered manner to adapt to smart and remote home medical care. In our recent researches, we found that electrical stimulation provided by wearable self-driven triboelectric nanogenerators (TENG) can regulate the catalytic properties of nanozymes with Fe-N<sub>4</sub> and Cu-N<sub>4</sub> active sites<sup>39,41</sup>, improving ROS production for cancer therapy. Based on electrostatic induction or contact electrification, TENG can convert mechanical energy in daily human activities into electrical pulses, providing a mild, safe, and self-manipulated electric field for electrical stimulation. These advances drive us to further explore how to improve the catalytic properties of nanozymes while improving their electro-responsiveness by fine manipulation of the intrinsic structure of nanozymes.

In this work, we modulate the electronic state of Ru-based nanozymes by facilely controlling the lattice spacing of Ru nanocrystals under various calcination temperatures (Fig. 1). We have found the lattice expansion can boost the responsiveness of the Ru nanozymes to electrical stimulation, realizing a maximum improvement in their catalytic activities to defeat cancer. The Ru nanozymes possess multienzyme-like activities, and the lattice expansion in Ru

nanocrystals enhances their catalytic activities and responsiveness to self-driven electrical stimulation. Through density functional theory (DFT) calculations, we analyze the mechanisms of lattice expansion and electrical stimulation in promoting the catalysis of RuX.

## Results

### Synthesis and characterization of RuX nanozymes

Ru nanozymes with different Ru lattice spacing were synthesized using a facile two-step method, employing zeolitic imidazolate framework-8 (ZIF8) as the supporting substrate (Fig. 1a). Initially, ruthenium acetylacetonate was mixed with Zn<sup>2+</sup> and 2-methylimidazole to produce ruthenium co-coordinated ZIF8 (Ru@ZIF8). Subsequently, the resultant product was carbonized under N<sub>2</sub> atmosphere at varying temperatures (800, 900, and 1000 °C), yielding RuX, where X represents the temperature of 800, 900, or 1000 °C. We also carbonized ZIF8 without Ru loading, referred as NC1000, to serve as a control sample for comparing activity and analyzing catalytic mechanism. From the scanning electron microscopy images, RuX exhibited a gradual decrease in particle size from 121.1 to 66.6 nm with increasing carbonization temperature from 800 to 1000 °C, all of which were much smaller than NC1000 (~205.1 nm) (Supplementary Fig. 1). Transmission electron microscope images revealed the trapezoidal dodecahedron shape of RuX nanoparticles with uneven distribution of small nanocrystals throughout the substrate. Additionally, selected area electron diffraction patterns exhibited their crystal structures (Fig. 2a, Supplementary Fig. 2a and Supplementary Fig. 3a). Surface and line-scan elemental mapping of C, N, O and Ru also proved the successful Ru loading into the substrate (Supplementary Fig. 2–Supplementary Fig. 4). The size of Ru nanocrystals displayed a slight increase from 3.06 nm to 3.52 nm as the carbonization temperature rose from 800 to 1000 °C (Supplementary Fig. 5). From the high-resolution transmission electron microscopy images, the lattice spacing of Ru nanocrystals gradually and uniformly expanded with higher carbonization temperatures, measuring 0.217 nm for Ru800, 0.225 nm for Ru900 and 0.230 nm for Ru1000 (Fig. 2b), representing expansion of 3.69% for Ru900 and 5.99% for Ru1000, respectively. We employed inductively coupled plasma optical emission spectroscopy to compare the Zn and Ru element contents in the RuX. The results revealed a gradual decrease in Zn content with increasing carbonization temperature, mainly attributed to thermal volatilization of Zn (Supplementary Table 1 and Supplementary Table 2). The Ru content in Ru900 and Ru1000 was similar (0.815 at% and 0.803 at%, respectively), approximately twice the content in Ru800 (0.424 at%). We tentatively deduced that at higher carbonization temperatures above the boiling point of Zn (907 °C), Zn gradually evaporated from the carbon matrix, potentially causing structural distortion of the carbon support and lattice expansion of Ru nanocrystals on the supports<sup>9,43,44</sup>. The lattice expansion in nanocrystals may induce local strain and electronic reconfiguration, altering the key functional properties substantially<sup>45–49</sup>.

We further employed X-ray diffraction (XRD) analysis to investigate their crystal structures (Fig. 2c). All RuX samples displayed two characteristic broad peaks at  $2\theta = 25^\circ$  and  $44^\circ$ , corresponding to the interlayer lattice planes of (002) and (101) graphite microcrystals of carbon, respectively. With increasing carbonization temperature, the intensity of the diffraction peak at  $44^\circ$  progressively rose, indicating increased graphitized carbon at higher temperatures<sup>50,51</sup>. Raman spectra results exhibited clear D and G bands at around  $1345\text{ cm}^{-1}$  and  $1581\text{ cm}^{-1}$  for all Ru nanozymes (Fig. 2d). As the carbonization temperature increased from 800 °C to 1000 °C, the I<sub>D</sub>/I<sub>G</sub> ratio gradually decreased from 1.875 to 1.24, signifying an elevated degree of graphitization, consistent with the XRD results. The chemical state in RuX was evaluated using X-ray photoelectron spectroscopy (XPS), revealing the presence of elements C, N, O, Zn, and Ru (Fig. 2e, Supplementary Table 2). High-resolution Ru 3p and 3d spectra confirmed the

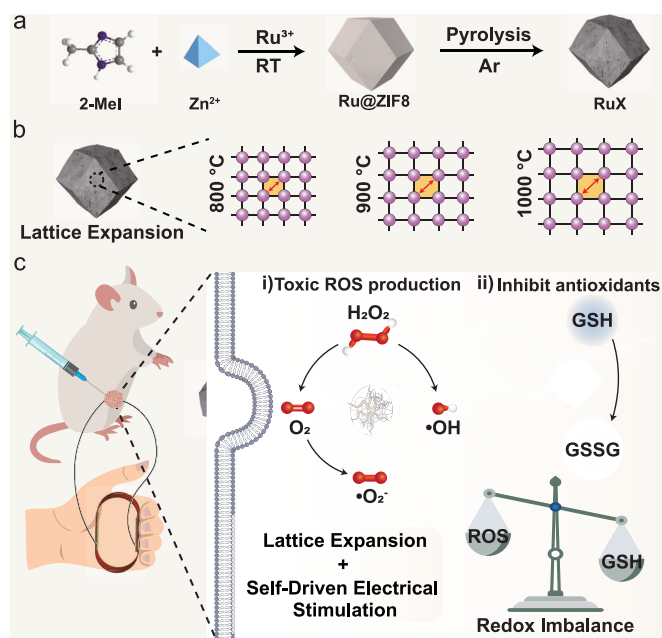


**Fig. 1 | Schematic diagram of the synthesis process of Ru nanozymes, temperature-induced lattice expansion and tumor therapy.** **a** Schematic diagram of the synthetic route of the Ru nanozymes (RuX, where X represents 800, 900, or 1000 °C). **b** Schematic diagram of lattice expansion of RuX with increasing pyrolysis temperature. **c** Schematic diagram of ROS production for enhanced oxidative stress of tumor by Ru nanozymes (RuX) under self-driven electric stimulation with triboelectric nanogenerator.

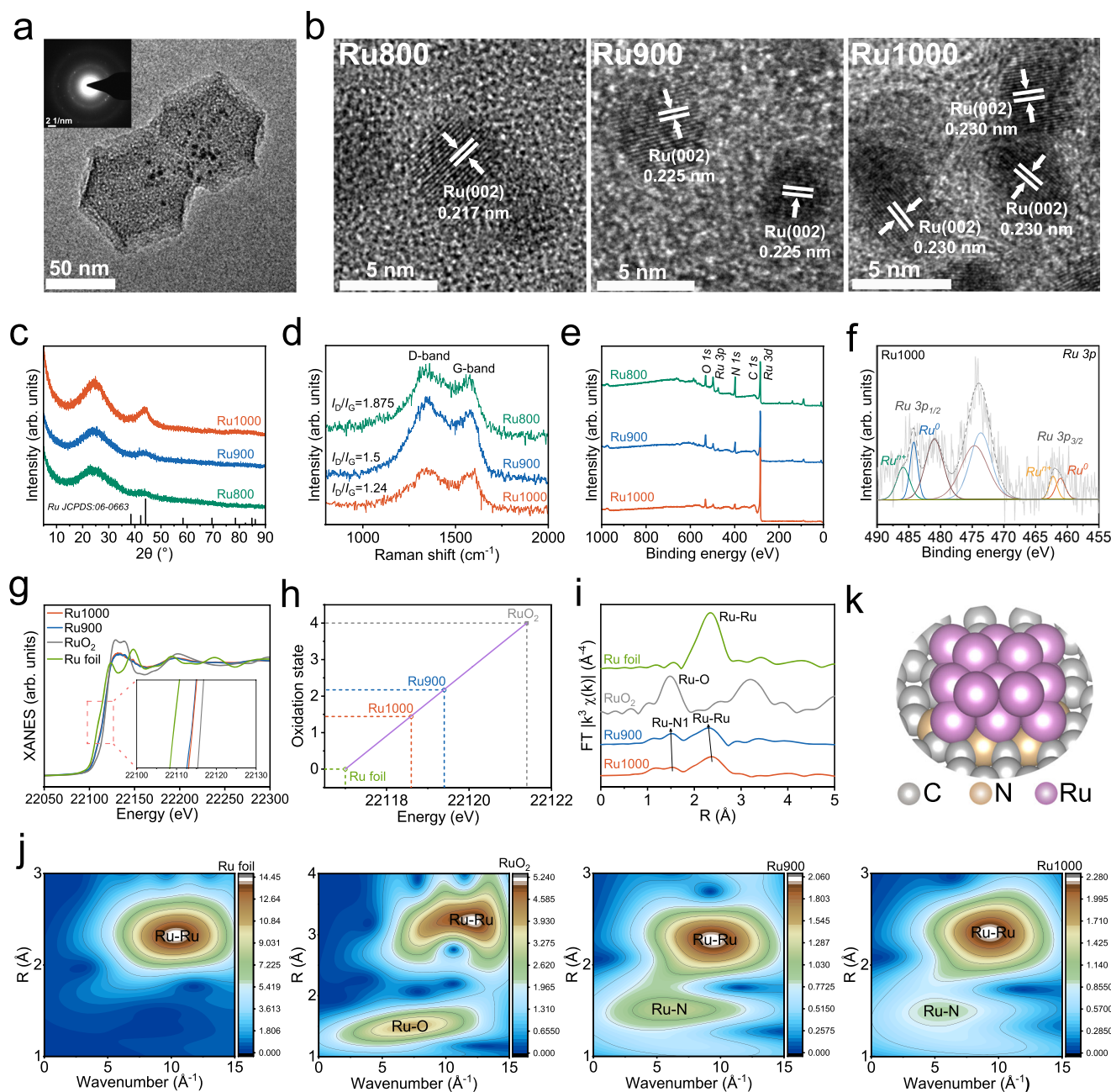


**Fig. 2 | Structural characterizations of RuX nanozymes. a** TEM image and selected area electron diffraction (SAED) pattern (inset) of Ru1000. **b** HR-TEM images of RuX (X = 800, 900, 1000, respectively). **c** XRD patterns of RuX. **d** Raman spectra of RuX. **e** XPS spectra of survey scan of RuX. **f** XPS spectrum of Ru 3p region of Ru1000. **g** Normalized XANES spectra of Ru1000, Ru900, RuO<sub>2</sub>, and Ru foil at Ru K-edge. Inset is the enlarged view of the pre-edge energy range of the samples. **h** Relationship between Ru K-edge absorption energy and valence states for

Ru1000, Ru900, Ru foil, and RuO<sub>2</sub>. **i** FT-EXAFS spectra of Ru1000, Ru900, RuO<sub>2</sub>, and Ru foil. **j** Wavelet transform of Ru foil, RuO<sub>2</sub>, Ru900, and Ru1000. **k** Schematic illustration showing structure of Ru nanocrystals on N-doped carbon substrate (Ru900 or Ru1000). In (a, b) the experiments were repeated independently three times with similar results, and a representative result is shown for each. Source data are provided as a Source Data file.

coexistence of multivalent Ru (0, +3, and +4) in the three RuX samples (Fig. 2f and Supplementary Fig. 6a). Notably, the existence of multivalent Ru may be attributed to the coordination between the surface Ru in the Ru nanocrystals and N in the substrate, or the unavoidable surface oxidation of metallic Ru nanocrystals<sup>52,53</sup>. In the C 1s spectrum, the three peaks located at 284.64, 285.34, and 287.54 eV were assigned to C-C, C=N and C-N bonds, respectively (Supplementary Fig. 6b, Supplementary Table 3)<sup>23,39</sup>. The N1s spectra displayed decomposition peaks corresponding to pyridinic N, pyrrole N, and graphite N. Moreover, an additional peak attributed to Ru-N coordination was observed

in the case of Ru1000. (Supplementary Fig. 6c, Supplementary Table 4).

With comparable Ru contents, we conducted further investigation into the fine electronic structure and coordination environment of Ru nanocrystals in Ru900 and Ru1000 using synchrotron radiation-based X-ray absorption near-edge structure (XANES) spectroscopy and extended X-ray absorption fine structure (EXAFS). The Ru K-edge XANES curves revealed that both Ru900 and Ru1000 exhibited higher energy absorption thresholds compared to Ru foil, yet lower than RuO<sub>2</sub> (Fig. 2g). The results indicated that the valence states of Ru



ranged from 0 to +4, suggesting a mixed local environment around Ru, which was consistent with the XPS results. Additionally, the average valence state of +1.44 in Ru1000 was lower than that of +2.17 in Ru900, indicating its closer resemblance to the metallic state (Fig. 2h). The EXAFS spectra displayed characteristic peaks of Ru-Ru bonds at 2.0–3.0 Å for both Ru900 and Ru1000, confirming the formation of Ru nanocrystals. Furthermore, compared to Ru900, the peak in Ru1000 displayed a slight redshift, indicating a slightly longer Ru-Ru bond length. Notably, a distinctive peak appeared at around 1.4 Å in Ru1000, which can be assigned to Ru–N coordination, as observed in its XPS spectrum (Fig. 2i).

Wavelet transforming of EXAFS was performed on Ru foil, RuO<sub>2</sub>, Ru900, and Ru1000 to investigate the dispersion of Ru on the N-doped carbon support (Fig. 2j). It is worth mentioning that the contour maps of both Ru900 and Ru1000 exhibited peaks at around 1.4 Å and 2.4 Å, corresponding to Ru–N and Ru–Ru coordination, respectively, indicating the presence of Ru particles. Quantitative EXAFS curve fitting results are displayed in Supplementary Fig. 7 and Supplementary Table 5. The coordination number of Ru–Ru bonds for Ru900 and Ru1000 were determined to be  $1.2 \pm 0.4$  and  $1.00 \pm 0.03$ , respectively, with average bond lengths of  $2.65 \pm 0.02$  Å and  $2.67 \pm 0.07$  Å, respectively. These findings suggested that the lattice expansion in Ru nanocrystals led to a slight increase in the Ru–Ru bond length, subsequently increasing the unsaturation of the Ru–Ru bonds. Additionally, the specific surface area of Ru800, Ru900, and Ru1000 assessed using nitrogen adsorption-desorption at 77.3 K were 679.1071, 703.2245, and 660.2020 m<sup>2</sup> g<sup>−1</sup>, respectively, and they possessed similar pore size distribution (Supplementary Fig. 8). Based on these findings, we roughly deduced the structure of Ru nanozymes (Ru900 and Ru1000). As shown in Fig. 2k, Ru nanocrystals are firmly anchored on the N-doped carbon substrate, and a portion of Ru atoms coordinate with nitrogen and carbon.

### Catalytic activities of RuX nanozymes

Similar to the active site distribution of natural metalloproteases with metal-amino acid coordination, transition metal-containing nanozymes often exhibit diverse enzymatic activities resembling those redox enzymes<sup>23,54–56</sup>. Here, we evaluated the enzyme-like activities of RuX, namely POD, OXD, CAT, and GSHOx activities, under weakly acidic pH condition that mimics the TME (Fig. 3a). RuX can be stably dispersed in aqueous solution within 10 days with negligible changes in hydrodynamic diameter and zeta potential (Supplementary Fig. 9), ensuring their stable catalysis. We detected the POD-like activity of RuX using 3,3',5,5'-tetramethylbenzidine (TMB) as the probe and H<sub>2</sub>O<sub>2</sub> as the substrate. The colorless TMB can be oxidized into blue oxTMB by •OH generated during the reaction<sup>57–59</sup>. As a result, control sample NC1000 without Ru nanocrystals exhibited negligible POD-like activity, while Ru800 with low Ru loading showed weak catalytic activity (Fig. 3b and Supplementary Fig. 10, Supplementary Table 1). In contrast, both Ru900 and Ru1000 demonstrated significantly higher POD-like activity, with Ru1000 exhibiting superior activity compared to Ru900 despite possessing similar Ru loading. This enhancement may be attributed to the lattice expansion of Ru nanocrystals in Ru1000. Additionally, we observed OXD-like activity in RuX, where O<sub>2</sub> was catalyzed to generate •O<sub>2</sub><sup>−</sup> in the absence of H<sub>2</sub>O<sub>2</sub>. Among the RuX samples, Ru1000 displayed the highest catalytic efficiency in generating •O<sub>2</sub><sup>−</sup> (Fig. 3c). The catalytic generation of •OH and •O<sub>2</sub><sup>−</sup> was further confirmed through electron spin resonance (ESR) measurement, as evident from the characteristic 1:2:2:1 four-line signals of •OH and the 1:1:1:1 four-line signals of •O<sub>2</sub><sup>−</sup> after capturing with 5,5-dimethyl-1-pyrroline-N-oxide (DMPO) (Fig. 3d, e). To intuitively observe the effect of lattice expansion on the rate of •OH generation catalyzed by RuX, we used time-dependent *in situ* ESR to monitor the generation process of •OH. Under the premise that the test conditions

were completely consistent, Ru1000 exhibited the highest reaction rate to generate •OH during the initial 120 s (Supplementary Fig. 11).

Moreover, we investigated the CAT-like and GSHOx-like activities of RuX (Fig. 3f, g). Consistently, Ru1000 demonstrated the highest enzyme-like activities. The O<sub>2</sub> produced through CAT-like activity can not only alleviate the hypoxic state in tumor tissues but also serve as a substrate for producing toxic •O<sub>2</sub><sup>−</sup> through the OXD-like activity of RuX. The GSHOx-like activities of RuX can destroy the intracellular antioxidant defense, amplifying oxidative damage. The mass spectrum (MS) verified the formation of the oxidation product oxidized glutathione (GSSH) and GSH was almost consumed at the 10th min (Supplementary Fig. 12). The cascade catalysis mediated by the four enzyme-like activities of RuX might cause a ROS storm that can finally boost cancer cell killing.

Subsequently, we investigated the steady-state kinetic process of RuX using Michaelis-Menten kinetics and Lineweaver-Burk plots (Supplementary Fig. 13 and Supplementary Fig. 14). The Michaelis constant ( $K_M$ ) and the maximum velocity ( $v_{max}$ ) of Ru1000 for the POD-like catalytic reaction were calculated as 18.4 mM and  $1.16 \times 10^{-6}$  M/s, respectively (Supplementary Table 6). Comparatively, the  $v_{max}$  of Ru1000 was 8.9 times higher than that of Ru800 and 1.15 times higher than that of Ru900, while the  $K_M$  of Ru1000 was lower than that of Ru800 and Ru900. These findings indicated that Ru1000 exhibited the highest affinity towards the substrate H<sub>2</sub>O<sub>2</sub>, effectively enhancing the generation rate of •OH. Similar results were observed in the kinetics of GSHOx-like catalytic reactions, where the  $v_{max}$  of Ru1000 was 3.11 and 1.23 times higher than Ru800 and Ru900, respectively (Supplementary Table 7). Based on these results, we deduced that lattice expansion in Ru nanocrystals positively regulated the catalytic activity of RuX.

In our previous studies, we demonstrated that the catalytic activity of nanozymes, including those supported on N-doped carbon, can be enhanced by self-driven electrical stimulation<sup>39–41</sup>. Building upon these findings, we further investigated whether self-driven electrical stimulation can also enhance the catalytic activities of RuX. To deliver the electrical stimulation, we fabricated a lightweight and wearable vertical contact-separation mode triboelectric nanogenerator (VCS-TENG) as a self-sustaining power source. The VCS-TENG was constructed using commonly used dielectric polytetrafluoroethylene film and copper-nickel alloy electrode with fabric rough structure for improving the contacting area and output performance (Fig. 3h). The resultant device can be manipulated by grasping and pressing with one hand, and the principle was shown in Supplementary Fig. 15a, b. Under reciprocating hand motion, VCS-TENG converts mechanical energy into electrical energy and generates alternating current. Specifically, when the VCS-TENG was pressed under a frequency of ~3 Hz, the open-circuit voltage ( $V_{oc}$ ) reached about 40 V, the short-circuit current ( $I_{sc}$ ) was ~3 μA, and the transferred charge was about 50 nC (Supplementary Fig. 15c–e). By applying different mechanical forces, the output  $V_{oc}$  can be adjusted within the range of 10–50 V (Fig. 3i). The output remained almost constant when the frequency was varied in the range of 1–4 Hz (Supplementary Fig. 15f). Even after ~4200 friction cycles within 1400 s, the  $V_{oc}$  value remained stable, indicating excellent stability of the VCS-TENG (Supplementary Fig. 15g). When the matching resistance was 20 MΩ, the maximum power generated by the VCS-TENG reached 81.9 μW (Supplementary Fig. 15h, i), providing a robust and biosafe electrical stimulation source.

We investigated the impact of electrical stimulation provided by VCS-TENG on the catalytic activities of RuX. First, we noticed that the POD-like activity of Ru1000 changed with the voltages and frequencies of the VCS-TENG and the pH values of the reaction media (Supplementary Fig. 16). Ru1000 exhibited optimal catalytic activity at a voltage of 50 V and a frequency of 3 Hz, so we selected this electrical stimulation parameter for subsequent exploration, and denoted this parameter as “E” if not otherwise specified. The results indicated that the application of electrical stimulation



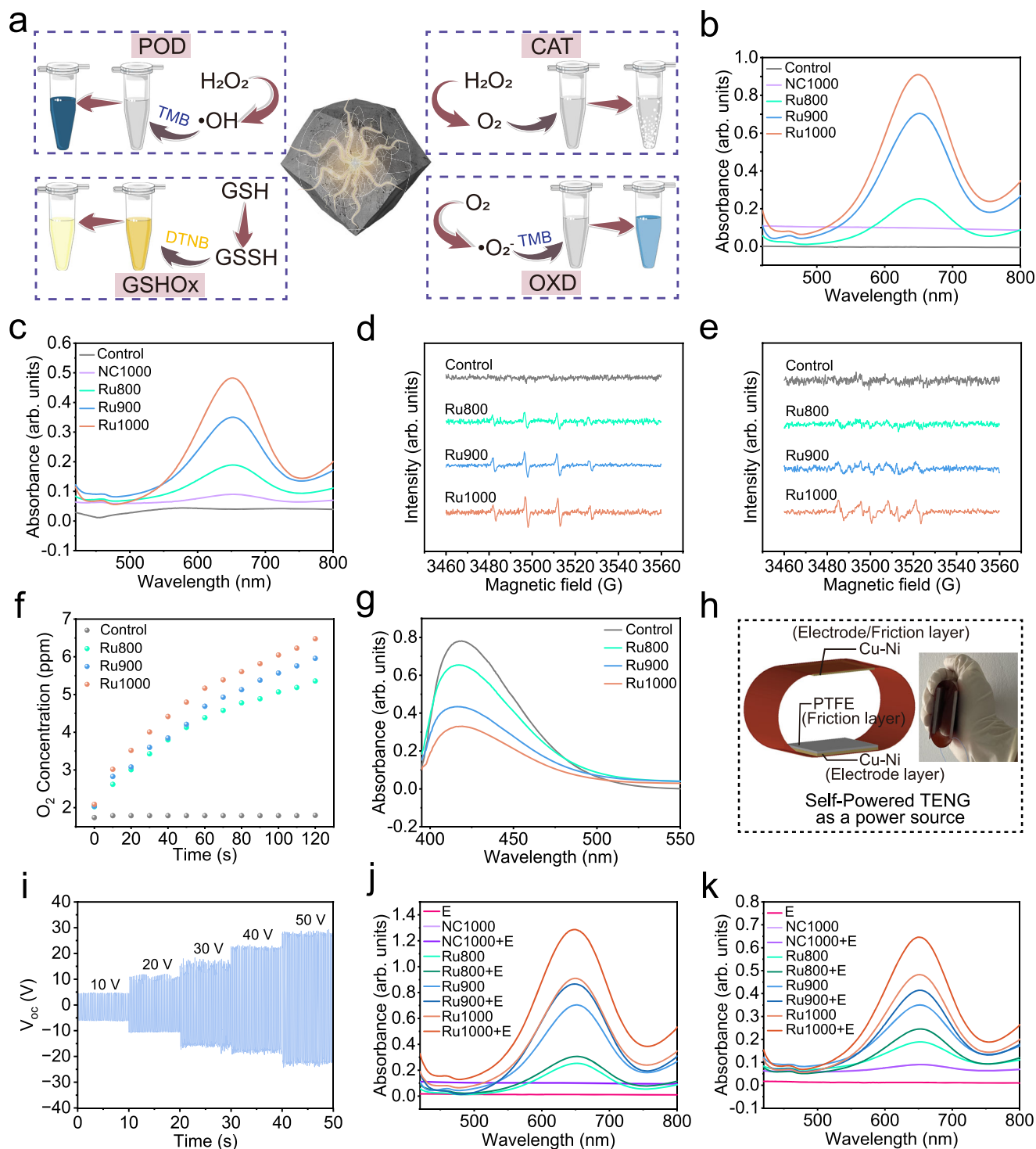


**Fig. 3 | Catalytic properties and electro-responsiveness of RuX.** **a** Schematic diagram of the catalytic reaction catalyzed by RuX. **b** Measurement of  $\cdot\text{OH}$  generation through POD-like activity using TMB as a probe. **c** Measurement of  $\cdot\text{O}_2^-$  generation through OXD-like activity using TMB as a probe. EPR spectra of **(d)**  $\cdot\text{OH}$  and **(e)**  $\cdot\text{O}_2^-$  trapped by 5,5-dimethyl-1-pyrroline-N-oxide (DMPO) at pH 6.5. **f** CAT-like activity of RuX decomposing  $\text{H}_2\text{O}_2$  to produce  $\text{O}_2$ . **g** GSHox-like activity under

various conditions. **h** Structural and optical photograph (inset) of VCS-TENG. **i** Output of VCS-TENG at different voltages. **j** Measurement of POD-like activity of RuX under electrical stimulation provided by VCS-TENG. **k** Measurement of OXD-like activity of RuX under electrical stimulation provided by VCS-TENG. Source data are provided as a Source Data file.

significantly improved the four distinct enzyme-like activities of all the RuX samples and ROS generation (Fig. 3j, k and Supplementary Fig. 17). Importantly, Ru1000 exhibited the most remarkable responsiveness to the electrical stimulation in regard to the catalytic efficiency. Compared to that without electrical stimulation, the POD-like catalytic efficiency of Ru1000 increased by 43.3%. In

contrast, Ru800 and Ru900 only increased by 20% and 24.3%, respectively. We speculated that the lattice expansion in Ru nanocrystals enhanced the electro-responsiveness of RuX. This hypothesis was supported by additional experiments involving terephthalic acid and methylene blue as the probes, which demonstrated that Ru1000 displayed the highest capability to

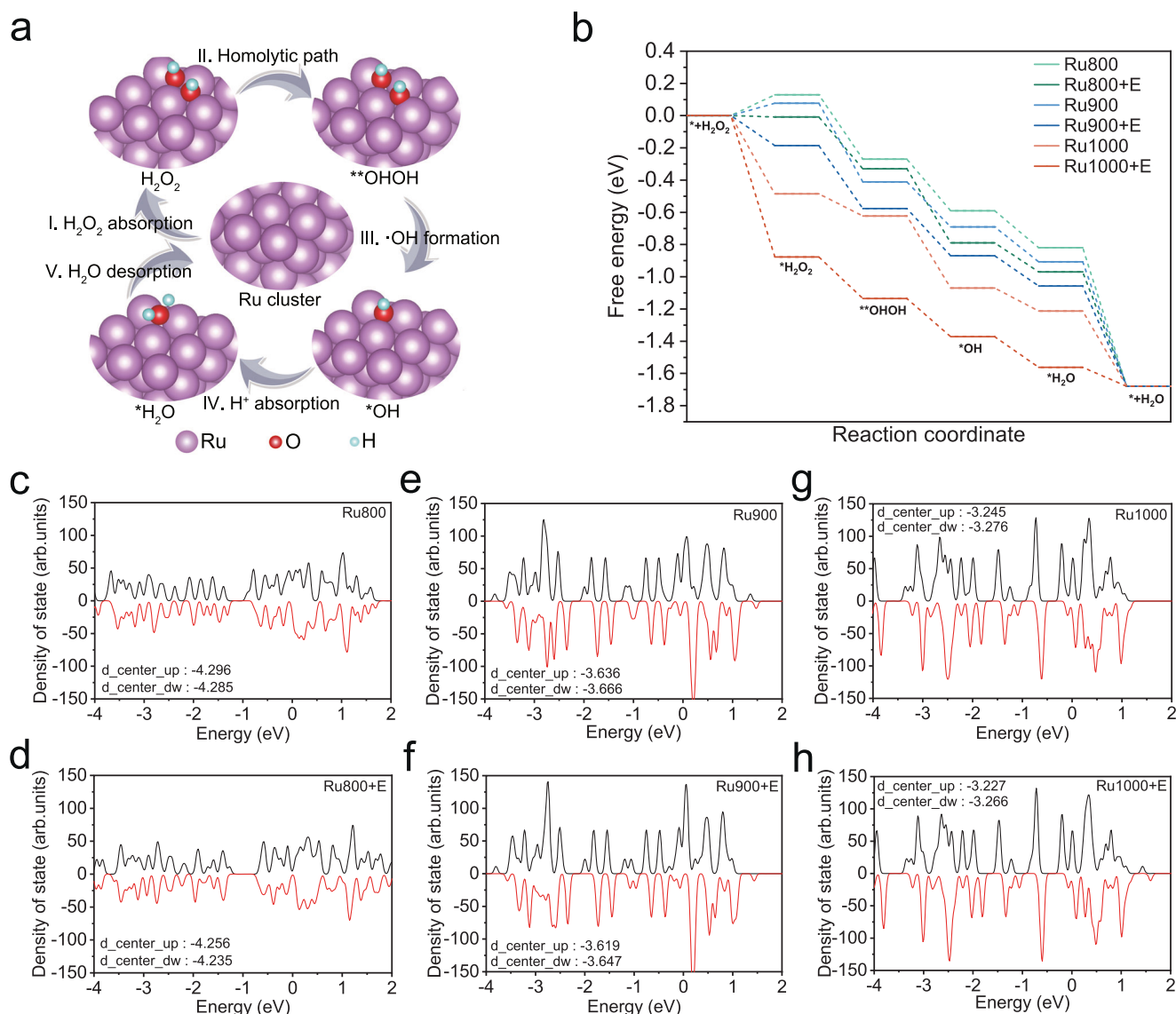


**Fig. 4 | DFT calculations of the promotion of the POD-like activity of RuX under lattice expansion and electrical stimulation. a** Proposed catalytic mechanism for POD-like reaction on RuX. **b** Corresponding free energy diagram for POD-like catalytic reaction on RuX under different conditions. DOS of Ru800 without electrical

stimulation (c) and with electrical stimulation (d). DOS of Ru900 without electrical stimulation (e) and with electrical stimulation (f). DOS of Ru1000 without electrical stimulation (g) and with electrical stimulation (h). Source data are provided as a Source Data file.

generate  $\cdot\text{OH}$  and  $\cdot\text{O}_2^-$  among all samples tested, and the electrical stimulation provided by VCS-TENG further improved the performance (Supplementary Fig. 17a, b). The ESR results confirmed that electrical stimulation efficiently promoted the generation of  $\cdot\text{OH}$  and  $\cdot\text{O}_2^-$  by Ru1000 (Supplementary Fig. 17c, d). In addition, the CAT-like and GSHOx-like activities of RuX also exhibited similar trend of electro-responsiveness (Supplementary Fig. 17e, f). We also explored its catalytic activities in cell culture media supplied with fetal bovine serum to simulate the actual cell growth environment. The results demonstrated that the Ru-based nanozymes can still maintain excellent four enzyme-like activities and electroresponsiveness, which had a consistent trend with the results detected in the phosphate buffered saline (PBS) (Supplementary Fig. 18). It suggested that the nanocatalysts can stably exert catalytic performance in various environments. We also used the same method to prepare copper-based nanozymes with different lattice spacings and found a similar phenomenon, that is, lattice expansion promotes the catalytic activity and electrical responsiveness of the

copper-based nanozymes (Supplementary Fig. 22). We will continue our research in our subsequent work.

### Mechanism of lattice expansion and electrical stimulation promoted catalysis

To elucidate the mechanism underlying the enhanced catalytic activities of Ru nanozymes induced by lattice expansion and electrical stimulation, we conducted DFT calculations. Figure 4a, b depicts the key intermediate structures and Gibbs free energy diagrams along the optimized reaction pathways for the  $\text{H}_2\text{O}_2$  to  $\cdot\text{OH}$  conversion, representative of the POD-like activity of RuX. Initially,  $\text{H}_2\text{O}_2$  molecules adsorb onto the active sites of the Ru nanocrystals. The adsorption energies on Ru800, Ru900 and Ru1000 are +0.13 eV, +0.1 eV, and -0.5 eV, respectively. For Ru800 and Ru900, the adsorption of  $\text{H}_2\text{O}_2$  is the rate-limiting step due to the higher lattice density and electron density, which impairs its ability to adsorb  $\text{H}_2\text{O}_2$ . In contrast, the adsorption of  $\text{H}_2\text{O}_2$  on Ru1000 is thermodynamically spontaneous without requiring additional energy. When an electric field is applied,

the adsorption energies on the surface of Ru800, Ru900, and Ru1000 all decrease, with the reduction of 0.14 eV, 0.27 eV, and 0.4 eV for Ru800, Ru900, and Ru1000, respectively. The corresponding free energy calculation results show that the order of adsorption difficulty of  $\text{H}_2\text{O}_2$  on the Ru surface is  $\text{Ru800} > \text{Ru900} > \text{Ru1000}$  (most difficult)  $< \text{Ru800} + \text{E} < \text{Ru900} + \text{E} < \text{Ru1000} + \text{E}$  (easiest). This demonstrates that both lattice expansion and electrical stimulation promote the reduction of electron density in the Ru nanocrystals, thereby facilitating binding with  $\text{H}_2\text{O}_2$  molecules. Notably, the overall reaction free energy decreases even further electrical stimulation is applied to Ru1000, indicating that lattice expansion amplifies the effect of electrical stimulation. This result is consistent with the kinetic data, where the  $K_M$  value representing the enzyme-substrate affinity is significantly reduced in Ru1000 compared to Ru900. In the second step, the adsorbed  $\text{H}_2\text{O}_2$  dissociates into two  $\cdot\text{OH}$ . Subsequently,  $\cdot\text{OH}$  desorbs from the Ru sites. Throughout this process, lattice expansion and electrical stimulation lower the energy barrier, favoring the formation of  $\cdot\text{OH}$ . The residual  $\cdot\text{OH}$  can then binds with H to form  $\text{H}_2\text{O}$  in acidic conditions. Finally, the Ru active sites return to their initial state after desorption of the  $\text{H}_2\text{O}$  molecules.

We conducted a comparison of the projected electronic densities of states between Ru800, Ru900, and Ru1000. Relative to Ru800 and Ru900, the d-band center of Ru1000 shifts closer to the Fermi level, resulting in a greater occupation of electrons near the Fermi energy level (Fig. 4c–h). Furthermore, under electrical stimulation, the d-band center of Ru1000 moves even closer to the Fermi level. These findings suggest that lattice expansion and electrical stimulation promote the transfer of active electrons during the catalytic process, facilitating the catalytic  $\cdot\text{OH}$  generation. Additionally, Supplementary Fig. 23 illustrates the adsorption energy of OH on the Ru nanocrystals. The calculated OH adsorption energies on Ru900, Ru900+E, Ru1000, and Ru1000+E are -0.90, -1.10, -1.38, and -1.63 eV, respectively. These results indicate that both lattice expansion and electrical stimulation enhance the Ru-OH bonding, favoring subsequent proton coupling reaction and accelerating the overall catalytic reaction.

We used in situ Raman spectroscopy to provide additional evidence for the fragmentation pathway of  $\text{H}_2\text{O}_2$ . Under the premise that the test conditions of the three samples were completely consistent, the intensity of the peak at  $3491\text{ cm}^{-1}$  from the stretching vibration of O-H in  $\text{H}_2\text{O}$  was strongest for Ru1000 and weakest for Ru800 (Supplementary Fig. 24). This was consistent with the step diagram results in DFT, indicating that the lattice expansion was conducive to accelerating the cracking process of  $\text{H}_2\text{O}_2$  during the catalytic reaction, ultimately promoting the generation of  $\cdot\text{OH}$ . Subsequently, we used cyclic voltammetry (CV) and electrochemical impedance spectroscopy to reveal the electron transfer process during the catalytic redox reaction of RuX and  $\text{H}_2\text{O}_2$ . Compared with Ru800 and Ru900, the current increase of Ru1000 were most significant, and prominent redox peaks appeared at bias voltages of -0.4 V and 0.2 V, which were attributed to the redox reaction from  $\text{H}_2\text{O}_2$  (Supplementary Fig. 25a). Interestingly, the current was further enhanced under the electrical stimulation provided by the VCS-TENG. The catalytic activity of Ru1000 was improved by the highest level under the electrical stimulation, followed by Ru900. Supplementary Fig. 25b displayed the Nyquist plots of Ru800, Ru900, and Ru1000 electrodes measured after supplying  $\text{H}_2\text{O}_2$ . The Nyquist curves of Ru900 and Ru1000 consisted of high-frequency curves and low-frequency linear parts, indicating that their redox reactions were dominated by charge transfer and diffusion processes. The high-frequency intercept can be partially attributed to charge transfer at the electrolyte/electrode interface. The charge transfer resistance obtained from the arc radius showed that Ru1000 had the lowest charge transfer resistance, and the redox reaction catalyzed by Ru1000 was easier. These results verified that the lattice expansion optimizes the first step of the redox reaction, that is, the adsorption of substrate  $\text{H}_2\text{O}_2$  on the active site occurs more easily.

Subsequently, it cooperates with external electrical stimulation to enhance the Ru-OH bonding, which is beneficial to the subsequent proton coupling reaction and accelerates the entire catalytic reaction.

### In vitro cancer therapy with Ru nanozymes

Encouraged by the capability of RuX to catalyze ROS generation and deplete GSH, we investigated their potential for killing cancer cells under electrical stimulation provided by the VCS-TENG (Fig. 5a). Initially, we evaluated the cytotoxicity of RuX on 4T1 cells using the 3-[4,5-dimethylthiazol-2-yl]-2,5-diphenyltetrazolium bromide (MTT) assay (Fig. 5b). Considering the overproduction of  $\text{H}_2\text{O}_2$  within tumors in vivo,  $\text{H}_2\text{O}_2$  (100  $\mu\text{M}$ ) was supplied to the cell culture medium to mimic the TME condition, which had no significant negative effect on cell viability ( $\text{H}_2\text{O}_2$  group in Fig. 5b). As a result, the cell viability of the Ru1000 group (200  $\mu\text{g/mL}$  of Ru1000) was found to be the lowest (36.25%) compared to the Ru800 and Ru900 groups. We also investigated the impact of electrical stimulation provided by VCS-TENG on cell viability. Applying electrical stimulation alone had no adverse effect on cell viability (E group in Fig. 5b). The cell viability of the Ru1000 + E group was the lowest, reaching 23.25%. Therefore, it can be concluded that Ru1000 exhibited the highest capacity for killing cancer cells, particularly under electrical stimulation. In addition, the cytotoxicity of Ru1000 was found to be concentration- and pH-dependent. The highest level of cell cytotoxicity was achieved at a Ru1000 concentration of 200  $\mu\text{g/mL}$ , in weakly acidic culture medium of pH 6.5, and with electrical stimulation applied (Fig. 5c). In contrast, after the treatment with 800  $\mu\text{g/mL}$  of Ru1000, the cell viability of normal mouse L929 fibroblasts was still higher than 65%, and there was no significant increase in toxicity after applying electrical stimulation (Fig. 5d). This indicated that Ru1000 and self-driven electricity had high biosafety when using for cancer therapy.

The anticancer efficacy of RuX was directly observed using live/dead cell staining with Calcein acetoxymethyl ester (Calcein-AM) and propidium iodide following various treatments (Supplementary Fig. 26). The percentages of viable cells in the E, Ru800, Ru900, and Ru1000 groups were determined to be 97.8%, 81.8%, 42.6%, and 32.4%, respectively. Notably, only 18.5% of cells remained viable in the Ru1000 + E group, indicating that Ru1000 demonstrated the highest cancer cell-killing potency when combined with electrical stimulation (Fig. 5e, f). To gain further insight into the cytotoxicity of RuX, intracellular ROS levels were assessed using 2',7'-dichlorodihydrofluorescein diacetate as a probe (Supplementary Fig. 27). The fluorescence increased in the Ru800, Ru900, Ru1000, and Ru1000 + E groups compared to the control group, confirming the ability of RuX to catalyze abundant ROS generation within the cells (Fig. 5g, h). Particularly, the Ru1000 + E group exhibited the strongest green fluorescence, indicating that Ru1000 can enhance ROS production under electrical stimulation, consequently leading to cellular oxidative damage and subsequent cell death. Moreover, mitochondrial membrane potential, indicative of mitochondrial damage, was visualized using 5,5',6,6'-tetrachloro-1,1',3,3'-tetraethylimidacarbocyanine iodide (JC-1) as a probe (Supplementary Fig. 28). As a result, the Ru1000 treated 4T1 cells exhibited prominent green fluorescence, which was further intensified in the Ru1000 + E group (Fig. 5i, j). These findings confirmed the severe oxidative damage to mitochondria induced by Ru1000 under electrical stimulation. This damage was attributed to the excessive production of ROS and the reduced antioxidative capacity of the cells, which can further activate the mitochondrial apoptotic pathway within the cells. Subsequently, GSH/GSSG detection kit was used to quantitatively determine the intracellular GSH contents. The GSH/GSSG molar ratio in intact 4T1 cells was -5.13, while after treatment with 200  $\mu\text{g mL}^{-1}$  Ru1000 for 12 h, the ratio dropped to -1.78 and further to -1.25 after additional electrical stimulation (Fig. 5k). It demonstrated that Ru1000 can eliminate GSH in cancer cells and destroy the antioxidant barrier and aggravate oxidative stress.



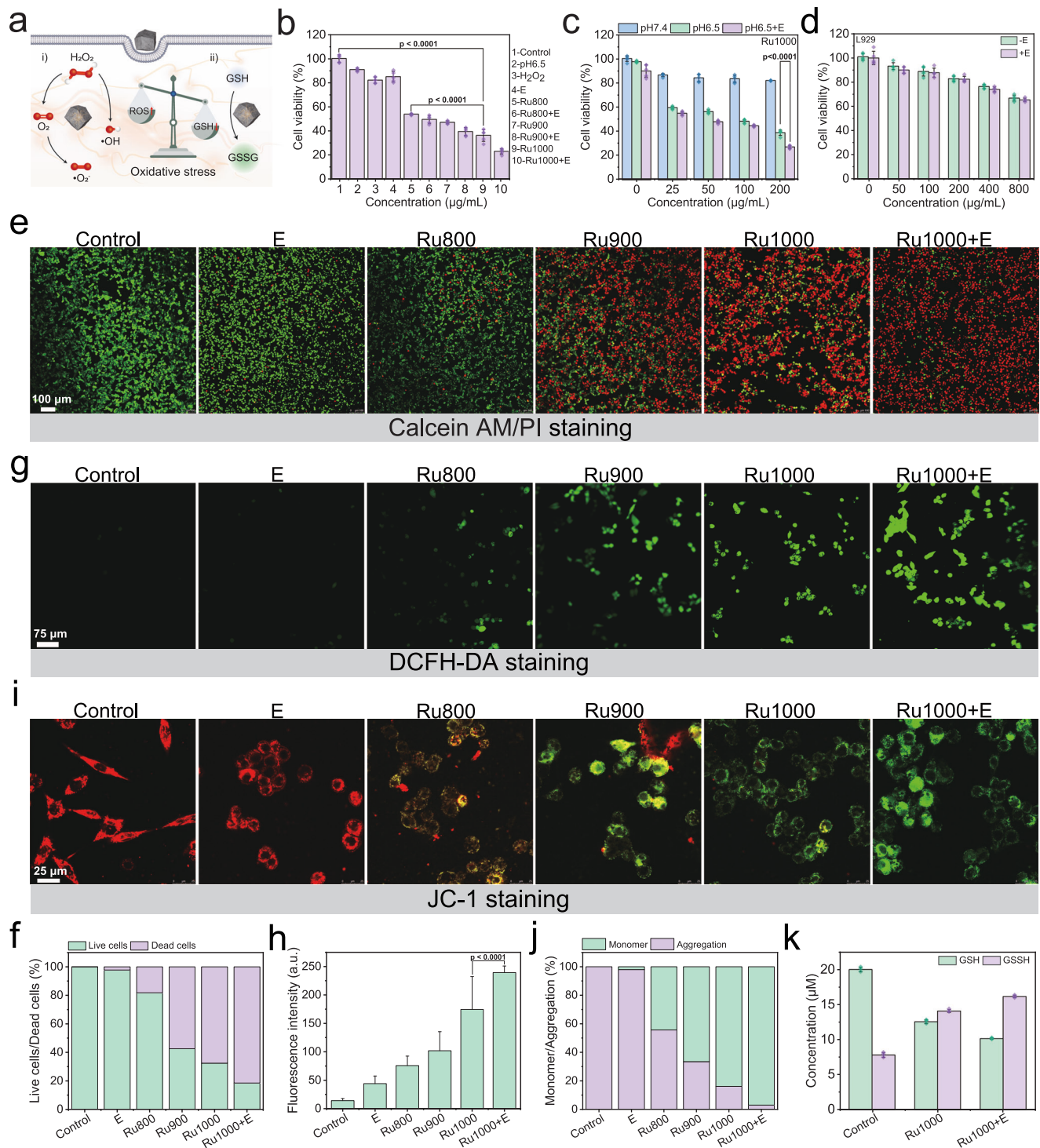


**Fig. 5 | Antitumor effect of RuX in vitro under self-driven electrical stimulation.** **a** Schematic illustration of RuX killing tumor cells via enzyme-like cascade reactions. **b** Viability of 4T1 cells under different conditions. Data are presented as mean values  $\pm$  SD ( $n = 5$  independent experiments). 4T1: murine mammary carcinoma cell line. **c** Viability of 4T1 cells after different treatments with Ru1000. Data are presented as mean values  $\pm$  SD ( $n = 5$  independent experiments). **d** Viability of L929 cells after treatment with different concentrations of Ru1000 with/without electrical stimulation. Data are presented as mean values  $\pm$  SD ( $n = 5$  independent experiments). L929: mouse fibroblast cell line. **e** Laser confocal images and **f** green/red fluorescence (FL) ratio of 4T1 cells stained with Calcein-AM (live cells:

green) and propidium iodide (dead cells: red) after various treatments. **g** Laser confocal images of intracellular ROS level stained with DCFH-DA in 4T1 cells and **h** corresponding quantitative data of intracellular ROS levels. Data are presented as mean values  $\pm$  SD. **i** JC-1 stained laser confocal image and **j** green/red FL ratios of 4T1 cells. **k** GSH/GSSG ratio in 4T1 cells before and after treatment with of Ru1000 ( $200 \mu g mL^{-1}$ ) and Ru1000 + E. Data are presented as mean values  $\pm$  SD ( $n = 3$  independent experiments). In (**e**, **g**, **i**) the experiments were repeated independently three times with similar results, and a representative result is shown for each. Source data are provided as a Source Data file.

### Acute toxicity of Ru1000 in mice

Based on the catalytic efficiency of RuX *in vitro* and at the cellular level, Ru1000 that exhibited the optimal therapeutic performance and high cytocompatibility was selected for further *in vivo* investigation. Prior to exploring its antitumor activity *in vivo*, a comprehensive assessment of systemic acute toxicity was conducted to demonstrate its biosafety. The result of hemolysis assay demonstrated that Ru1000 had a low hemolysis rate at a concentration high up to 800  $\mu\text{g/mL}$ , suggesting high hemocompatibility (Supplementary Fig. 29). The acute toxicity test was conducted by administering different doses of Ru1000 (0, 50, 100, and 200 mg/kg) into female BALB/c mice via intravenous injection. Over a 14-days observation period, no abnormal clinical signs were observed in any of the mice, and the body weight changes in the treatment groups followed a pattern similar to that of the control group (Supplementary Fig. 30).

Fourteen days after the intravenous injection, blood biochemistry tests revealed that hepatic and renal function markers, including alanine aminotransferase, aspartate aminotransferase, blood urea nitrogen, and creatinine, showed no abnormal changes in the mice injected with Ru1000 compared to the control group (Supplementary Fig. 31a). Furthermore, the blood routine test revealed that white blood cell, red blood cell, hemoglobin, mean corpuscular volume, mean corpuscular hemoglobin, mean corpuscular hemoglobin concentration, hematocrit, and platelets remained within normal ranges across various doses of Ru1000 (Supplementary Fig. 31b). Finally, hematoxylin and eosin (H&E) staining of major organs, including the heart, liver, spleen, lungs, and kidneys in all mice, revealed no histological abnormalities, confirming the excellent biocompatibility of Ru1000 (Supplementary Fig. 31c).

### In vivo cancer therapy with Ru1000

Encouraged by the excellent tumor killing *in vitro*, a subcutaneous 4T1 tumor-bearing BALB/c mice were employed to evaluate the *in vivo* anticancer effect of Ru1000. The tumor-bearing mice were randomly divided into four groups ( $n=6$ ): (1) control group: receiving local injection of PBS; (2) E group: exposed to electrical stimulation generated by VCS-TENG, which was manipulated by an experimental operator; (3) Ru1000 group: locally injected with 5 mg/kg Ru1000; (4) Ru1000 + E group: receiving local injection of 5 mg/kg Ru1000 followed by electrical stimulation using VCS-TENG. During the 14-day treatment period, the mice received a single Ru1000 administration on day 0, followed by a single electrical stimulation after 6 h (Fig. 6a). Analysis of the tumor growth curves during the treatment revealed rapid tumor growth in the E group, with no significant difference compared to the control group (Fig. 6b, c). Notably, the Ru1000 group exhibited obvious tumor suppression, attributed to the excellent catalytic activity of Ru1000. More importantly, the Ru1000 + E group demonstrated the highest tumor suppression effect, suggesting that the electrical stimulation provided by VCS-TENG efficiently enhanced the therapeutic efficacy of Ru1000. At the end of the treatment, the tumor suppression rates were calculated as 61% and 82% in the Ru1000 and Ru1000 + E groups, respectively, based on the tumor weights (Fig. 6d, e).

Throughout the treatment, there were no significant differences in the changes of body weight among all mice, indicating the high biological safety of the treatment method (Supplementary Fig. 32). Pathological examination through H&E staining revealed that the residual tumor tissues in the Ru1000 + E group exhibited the largest area of tumor necrosis (Fig. 6f). Furthermore, immunohistochemical staining of Ki-67, a key marker associated with active cancer cell proliferation, displayed a similar trend (Fig. 6f). Additionally, H&E staining of major organs including the heart, liver, spleen, lungs, and kidneys showed no apparent abnormalities or inflammation (Supplementary Fig. 33). These results confirmed the excellent catalytic activity and electro-responsiveness of Ru1000 for effective cancer therapy with good biosafety.

### Discussion

In summary, we demonstrate that Ru lattice expansion and external electrical stimulation can significantly enhance the catalytic activity of ruthenium-based nanozymes. Under pyrolysis temperature of 1000  $^{\circ}\text{C}$ , the lattice spacing of Ru nanocrystals supporting on N-doped carbon substrates expands by 5.99%, enhancing the catalytic activities of POD, CAT, OXD, and GSHOx-like enzymes to form cascade catalytic reactions for amplifying the oxidative damage and death of cancer cells. We find that a self-propelled electrical field provided by TENG can further improve the catalytic activities and the electro-responsiveness of RuX is highest when the lattice spacing of Ru nanocrystals reaches 0.23 nm. DFT results prove that the lattice expansion and external electrical stimulation can reduce the electron density of the nanozymes and shift the d-band center towards Fermi level, effectively enhancing the adsorption capacity of the substrate and lower the energy barrier. This work opens horizons for catalytic optimization of nanozymes.

### Methods

#### Ethical regulations

BALB/c female mice aged about 6 weeks were provided by Beijing Vital River Laboratory Animal Technology Co., Ltd., and the animal handling procedures were in strict compliance with the Beijing Administration Rule of Laboratory Animals and the national standards Laboratory Animal Requirements of Environment and Housing Facilities (GB 14925-2001). The animal experiments were approved by the Committee on Ethics of Beijing Institute of Nanoenergy and Nanosystems (Approval Number: 2022A043). All mice were group-housed five mice per cage in a specific pathogen-free environment in temperature (22–26  $^{\circ}\text{C}$ ) and humidity (40–70%) house rooms on a 12 h light, 12 h dark cycle. The maximum tumor diameter allowed by the Ethics Committee of Beijing Institute of Nanoenergy and Nanosystems is 15 mm, and no mice in this experiment exceeded this standard.

#### Preparation of RuX ( $X=800, 900$ , or 1000)

For the preparation of RuX (with  $X$  values of 800, 900, and 1000),  $\text{Zn}(\text{NO}_3)_2 \cdot 6\text{H}_2\text{O}$  and ruthenium acetylacetonate were dissolved in 15 ml of methanol. The resulting solution was then added dropwise into 10 mL of methanol containing 2-methylimidazole under stirring. After vigorous stirring for 5 min, the mixed solution was left at room temperature overnight. The product, Ru@ZIF8, was collected by centrifugation at 15,493  $g$ , washed three times with methanol, and dried under vacuum overnight. Subsequently, the dried solid powder was transferred to a tube furnace and heated to temperature of 800  $^{\circ}\text{C}$ , 900  $^{\circ}\text{C}$ , and 1000  $^{\circ}\text{C}$  under a flowing nitrogen atmosphere at a heating rate of 5  $^{\circ}\text{C min}^{-1}$ . The samples were held at these temperatures for 180 min, before being naturally cooled to room temperature to obtain Ru800, Ru900, and Ru1000, respectively.

#### GSHOx-like activity and kinetic assay

GSHOx-like activity was determined using DTNB as a probe, which reacts with thiol groups ( $-\text{SH}$ ) in GSH to produce a yellow product with an absorption maximum at 412 nm. Specifically, RuX (30  $\mu\text{g/mL}$ ) was reacted with GSH (0.3 mM) in a pH 6.5 PBS buffer, and the absorbance of the solutions at 412 nm was measured after 19 min. Subsequently, the content of GSH and GSSH in the reaction system was dynamically detected through MS. Briefly, the reaction solution was taken at the 1st, 5th, and 10th min for testing. Finally, the kinetics of GSHOx-like activity were measured by reacting RuX (30  $\mu\text{g/mL}$ ) with various concentrations of GSH (0.2 mM, 0.3 mM, 0.4 mM, and 0.5 mM). The kinetic parameters were calculated using the aforementioned formulas ( $\epsilon=13600 \text{ M}^{-1} \text{ cm}^{-1}$  for TNB). To prevent oxidation of GSH under light, all experiments were carried out in the dark.



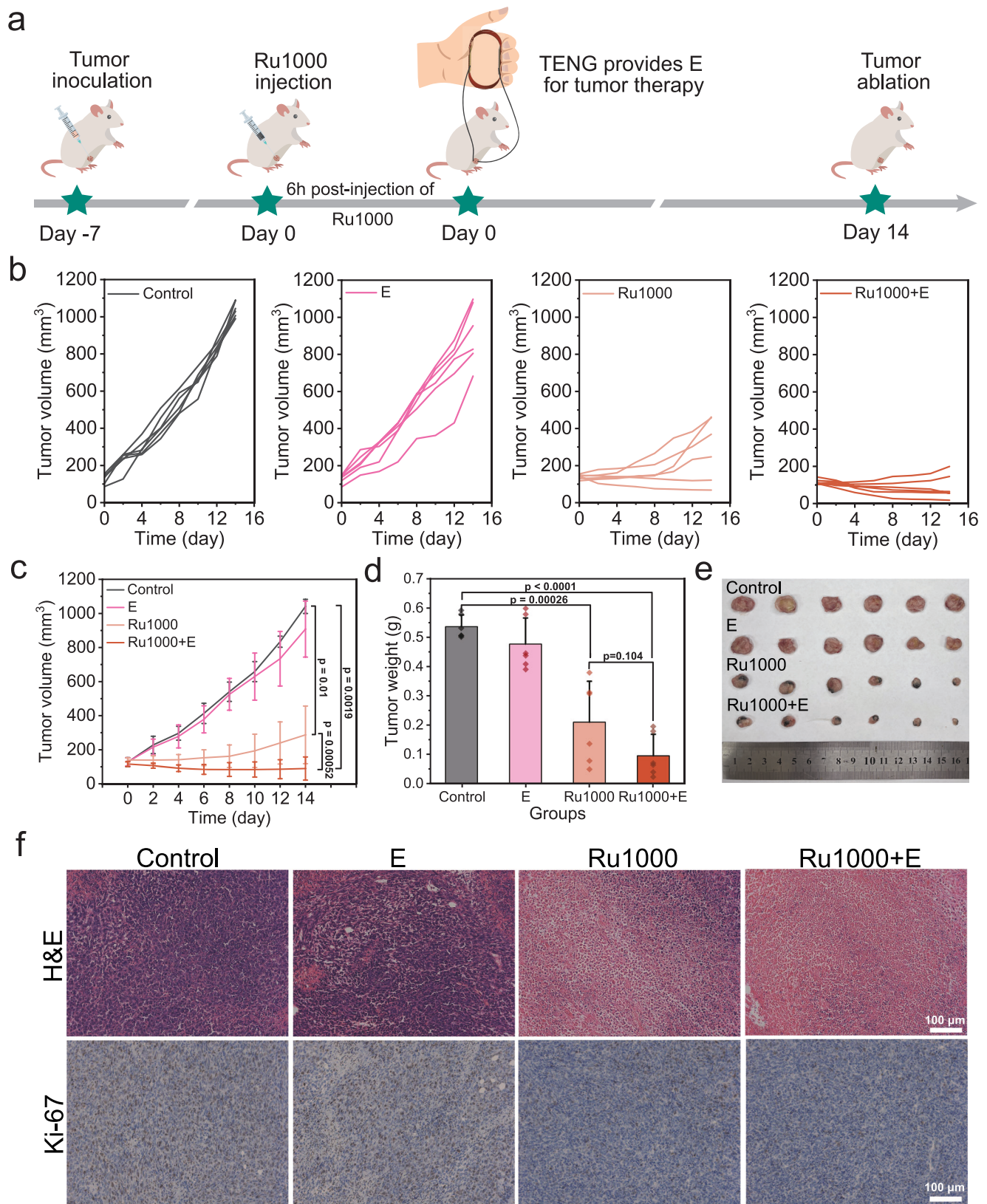


**Fig. 6 | In vivo antitumor effect of Ru1000.** **a** Schematic representation depicting the treatment procedure of 4T1 tumor mice by local injection of Ru1000 and electrical stimulation provided by VCS-TENG. **b** Individual tumor growth curves of the mice after various treatments. **c** Tumor growth curves of mice subjected to various treatments. Data are presented as mean values  $\pm$  SD ( $n = 6$  independent

experiments). **d** Average weight of tumors after 14 days of treatments. Data are presented as mean values  $\pm$  SD ( $n = 6$  independent experiments). **e** Optical photograph displaying the excised tumors on day 14. **f** H&E and Ki-67 staining of tumor sections from different groups. Source data are provided as a Source Data file.



## Detection of ROS by ESR

For the ESR assay, DMPO was used as a  $\cdot\text{OH}$  and  $\cdot\text{O}_2^-$  trapping agent. RuX (30  $\mu\text{g/mL}$ ) was added to pH 6.5 PBS containing  $\text{H}_2\text{O}_2$  (10 mM) and DMPO (100  $\mu\text{M}$ ). The mixture was then aspirated with a capillary tube for ESR detection.

## MTT assay

Biocompatibility of Ru1000 was assessed using L929 cell as a normal cell model. The cells were seeded in 96-well plates at a density of 5000 cells per well in 200  $\mu\text{L}$  of DMEM medium. Various concentrations of Ru1000 (25  $\mu\text{g/mL}$ , 50  $\mu\text{g/mL}$ , 100  $\mu\text{g/mL}$ , 200  $\mu\text{g/mL}$ , 400  $\mu\text{g/mL}$ , and 800  $\mu\text{g/mL}$ ) was added to each well. After 24 h of incubation, 20  $\mu\text{L}$  of MTT solution was added to each well. After additional 4 h, the liquid was aspirated, and 150  $\mu\text{L}$  of DMSO was added to each well, and 100  $\mu\text{L}$  of the supernatant was collected to measure the absorbance at 490 nm using a microplate reader.

For therapy, 4T1 cells were seeded into 96-well plates at a density of 5000 cells per well in 200  $\mu\text{L}$  of normal DMEM medium. After 24 h of culture, the medium was removed, and Ru1000 dissolved in weakly acidic medium (pH 6.5) was added to the wells at concentrations of 25  $\mu\text{g/mL}$ , 50  $\mu\text{g/mL}$ , 100  $\mu\text{g/mL}$ , and 200  $\mu\text{g/mL}$ . Following a 6-h incubation, 20  $\mu\text{L}$  of  $\text{H}_2\text{O}_2$  (100  $\mu\text{M}$ ) was added to each well, and the cells in the Ru1000 + E group were immediately subjected to electrical stimulation (50 V for 5 min). The cells were incubated for additional 20 h after completing the stimulation. The cell viability was assessed using the MTT assay.

## Cell fluorescence imaging

Cell fluorescence images were acquired using a confocal laser scanning microscopy (CLSM) (Leica SP8), and relative fluorescence intensities were determined by Image J software. 4T1 cells were seeded on glass-bottom dishes at a density of  $8 \times 10^4$  cells per well in 2 mL of DMEM medium and incubated for 24 h. The groups included untreated (control), E (50 V), Ru800 (200  $\mu\text{g/mL}$ ), Ru900 (200  $\mu\text{g/mL}$ ), Ru1000 (200  $\mu\text{g/mL}$ ), and Ru1000 + E (200  $\mu\text{g/mL}$ , 50 V). For live and dead cell analysis, after treatment under the different conditions, the cells were stained using Calcein-AM and PI and observed on CLSM to differentiate live and dead cells.

## For detection of intracellular ROS level, 4T1 cells after different treatments were stained with DCFH-DA for 30 min

Mitochondrial membrane potential was measured by adding JC-1 to differently treated 4T1 cells. After a 20 min incubation, red fluorescent JC-1 aggregates and green fluorescent JC-1 monomers were observed.

## In vivo acute toxicity

Twelve female BALB/c mice, 8 weeks old with body weights of  $\sim 20$  g, were randomly divided into four groups. The mice in each group were intravenously injected with 0, 50, 100 or 200  $\text{mg kg}^{-1}$  of Ru1000 dissolved in PBS. Over a 14-day evaluation period, the normal activity, health status, food intake, water intake and body weight of the mice were recorded. After 14 days, blood routine and blood biochemical indexes were analyzed. The mice were euthanized by painless cervical dislocation, and histopathological analysis of major organs (heart, liver, spleen, lung, and kidney) was performed.

## Statistical analysis

All experiments were expressed as mean values  $\pm$  S.D. Statistical differences were calculated using the two-tailed Student's *t* test.

## Reporting summary

Further information on research design is available in the Nature Portfolio Reporting Summary linked to this article.

## Data availability

Data supporting the findings of this work are available within the paper and its Supplementary Information files. Source data are provided with this paper. The full image dataset is available from the corresponding author upon request. Source data are provided with this paper.

## References

- Gao, W. et al. Deciphering the catalytic mechanism of superoxide dismutase activity of carbon dot nanozyme. *Nat. Commun.* **14**, 160 (2023).
- Yang, W. et al. Nanozymes: activity origin, catalytic mechanism, and biological application. *Coord. Chem. Rev.* **448**, 214170 (2021).
- Das, B. et al. Nanozymes in point-of-care diagnosis: an emerging futuristic approach for biosensing. *Nanomicro Lett.* **13**, 1–51 (2021).
- Jiang, D. et al. Nanozyme: new horizons for responsive biomedical applications. *Chem. Soc. Rev.* **48**, 3683–3704 (2019).
- Mei, L. et al. An overview of the use of nanozymes in antibacterial applications. *Chem. Eng. J.* **418**, 129431 (2021).
- Wang, H., Wan, K. & Shi, X. Recent advances in nanozyme research. *Adv. Mater.* **31**, 1805368 (2019).
- Tang, G., He, J., Liu, J., Yan, X. & Fan, K. Nanozyme for tumor therapy: surface modification matters. *Exploration* **1**, 75–89 (2021).
- Fan, K. et al. In vivo guiding nitrogen-doped carbon nanozyme for tumor catalytic therapy. *Nat. Commun.* **9**, 1440 (2018).
- Xia, F. et al. Ultrasmall ruthenium nanoparticles with boosted anti-oxidant activity upregulate regulatory T cells for highly efficient liver injury therapy. *Small* **18**, 2201558 (2022).
- Ghosh, S., Roy, P., Karmodak, N., Jemmis, E. D. & Magesh, G. Nanosozymes: crystal-facet-dependent enzyme-mimetic activity of V2O5 nanomaterials. *Angew. Chem.* **130**, 4600–4605 (2018).
- Fang, G. et al. Differential Pd-nanocrystal facets demonstrate distinct antibacterial activity against gram-positive and gram-negative bacteria. *Nat. Commun.* **9**, 129 (2018).
- Singh, N., Savanur, M. A., Srivastava, S., D'Silva, P. & Magesh, G. A redox modulatory  $\text{Mn}_3\text{O}_4$  nanozyme with multi-enzyme activity provides efficient cytoprotection to human cells in a Parkinson's disease model. *Angew. Chem.* **129**, 14455–14459 (2017).
- Ding, Y. et al. Enhanced sonodynamic cancer therapy through iron-doping and oxygen-vacancy engineering of piezoelectric bismuth tungstate nanosheets. *Small* **19**, 2300327 (2023).
- Zhang, R. et al. Edge-site engineering of defective Fe-N4 nanozymes with boosted catalase-like performance for retinal vasculopathies. *Adv. Mater.* **34**, 2205324 (2022).
- Li, A., Zhang, M., Ma, W., Li, D. & Xu, Y. Sugar-disguised bullets for combating multidrug-resistant bacteria infections based on an oxygen vacancy-engineered glucose-functionalized  $\text{MoO}_3$ -x photo-coordinated bienzyme. *Chem. Eng. J.* **431**, 133943 (2022).
- Wang, L. et al. Defect-rich adhesive molybdenum disulfide/rGO vertical heterostructures with enhanced nanozyme activity for smart bacterial killing application. *Adv. Mater.* **32**, 2005423 (2020).
- Chen, Y., Chen, T., Wu, X. & Yang, G. Oxygen vacancy-engineered pegylated  $\text{MoO}_3$ -x nanoparticles with superior sulfite oxidase mimetic activity for vitamin B1 detection. *Small* **15**, 1903153 (2019).
- Zhang, S. et al. Single-atom nanozymes catalytically surpassing naturally occurring enzymes as sustained stitching for brain trauma. *Nat. Commun.* **13**, 4744 (2022).
- Xu, B. et al. A bioinspired five-coordinated single-atom iron nanozyme for tumor catalytic therapy. *Adv. Mater.* **34**, 2107088 (2022).
- Ji, S. et al. Matching the kinetics of natural enzymes with a single-atom iron nanozyme. *Nat. Catal.* **4**, 407–417 (2021).
- Chang, M. et al. Single-atom Pd nanozyme for ferroptosis-boosted mild-temperature photothermal therapy. *Angew. Chem. Int. Ed.* **60**, 12971–12979 (2021).

22. Chen, Y. et al. Hierarchically porous S/N codoped carbon nanozymes with enhanced peroxidase-like activity for total antioxidant capacity biosensing. *Anal. Chem.* **92**, 13518–13524 (2020).
23. Ye, J. et al. Tumor response and NIR-II photonic thermal co-enhanced catalytic therapy based on single-atom manganese nanozyme. *Adv. Funct. Mater.* **32**, 2206157 (2022).
24. Chen, X. et al. Single-stranded DNA-encoded gold nanoparticle clusters as programmable enzyme equivalents. *J. Am. Chem. Soc.* **144**, 6311–6320 (2022).
25. Han, L., Zhang, H., Chen, D. & Li, F. Protein-directed metal oxide nanoflakes with tandem enzyme-like characteristics: colorimetric glucose sensing based on one-pot enzyme-free cascade catalysis. *Adv. Funct. Mater.* **28**, 1800018 (2018).
26. Liu, B. & Liu, J. Surface modification of nanozymes. *Nano Res.* **10**, 1125–1148 (2017).
27. Hu, X. et al. Biodegradation-mediated enzymatic activity-tunable molybdenum oxide nanourchins for tumor-specific cascade catalytic therapy. *J. Am. Chem. Soc.* **142**, 1636–1644 (2019).
28. Wang, H. et al. Disentangling the size-dependent geometric and electronic effects of palladium nanocatalysts beyond selectivity. *Sci. Adv.* **5**, eaat6413 (2019).
29. Ding, X. et al. Activity regulating strategies of nanozymes for biomedical applications. *Small* **19**, 2207142 (2023).
30. Xu, Y. et al. The Fe-N-C nanozyme with both accelerated and inhibited biocatalytic activities capable of accessing drug–drug interactions. *Angew. Chem. Int. Ed.* **59**, 14498–14503 (2020).
31. Huang, L., Chen, J., Gan, L., Wang, J. & Dong, S. Single-atom nanozymes. *Sci. Adv.* **5**, eaav5490 (2019).
32. Cen, D. et al. A near-infrared light-responsive ros cascade nano-platform for synergistic therapy potentiating antitumor immune responses. *Adv. Funct. Mater.* **33**, 2211402 (2023).
33. Wang, T. et al. Boosting h<sub>2</sub>O<sub>2</sub>-guided chemodynamic therapy of cancer by enhancing reaction kinetics through versatile biomimetic fenton nanocatalysts and the second near-infrared light irradiation. *Adv. Funct. Mater.* **30**, 1906128 (2020).
34. Lian, Z. et al. Near infrared light induced plasmonic hot hole transfer at a nano-heterointerface. *Nat. Commun.* **9**, 2314 (2018).
35. Zhao, Y. et al. Piezotronic and piezo-phototronic effects on sonodynamic disease therapy. *BME Mat* **1**, e12006 (2023).
36. Zhao, Y. et al. Manganese oxide-modified bismuth oxychloride piezoelectric nanoplatform with multiple enzyme-like activities for cancer sonodynamic therapy. *J. Colloid Interface Sci.* **640**, 839–850 (2023).
37. Zhao, Y. et al. Piezotronic effect-augmented Cu<sub>2-x</sub>O/BaTiO<sub>3</sub> sonosensitizers for multifunctional cancer dynamic therapy. *ACS Nano* **16**, 9304–9316 (2022).
38. Ge, M. et al. Magnetostrictive-piezoelectric-triggered nanocatalytic tumor therapy. *Nano Lett.* **21**, 6764–6772 (2021).
39. Zhong, S. et al. Self-driven electricity modulates d-band electrons of copper single-atom nanozyme for boosting cancer therapy. *Adv. Funct. Mater.* **33**, 2305625 (2023).
40. Yao, S. et al. Self-driven electrical stimulation promotes cancer catalytic therapy based on fully conjugated covalent organic framework nanocages. *Adv. Funct. Mater.* **32**, 2209142 (2022).
41. Yao, S. et al. Bioinspired electron polarization of nanozymes with a human self-generated electric field for cancer catalytic therapy. *Adv. Mater.* **34**, 2109568 (2022).
42. Gu, T. et al. Platinum nanoparticles to enable electrodynamic therapy for effective cancer treatment. *Adv. Mater.* **31**, 1806803 (2019).
43. Qi, Z. et al. Conversion of confined metal@ ZIF-8 structures to intermetallic nanoparticles supported on nitrogen-doped carbon for electrocatalysis. *Nano Res.* **11**, 3469–3479 (2018).
44. Bai, L. et al. Explaining the size dependence in platinum-nano-particle-catalyzed hydrogenation reactions. *Angew. Chem. Int. Ed.* **55**, 15656–15661 (2016).
45. Xie, M., Zhang, B., Jin, Z., Li, P. & Yu, G. Atomically reconstructed palladium metallene by intercalation-induced lattice expansion and amorphization for highly efficient electrocatalysis. *ACS Nano* **16**, 13715–13727 (2022).
46. Liu, G. et al. Hydrogen-intercalation-induced lattice expansion of Pd@ Pt core-shell nanoparticles for highly efficient electrocatalytic alcohol oxidation. *J. Am. Chem. Soc.* **143**, 11262–11270 (2021).
47. Chen, C. et al. Large local lattice expansion in graphene adlayers grown on copper. *Nat. Mater.* **17**, 450–455 (2018).
48. He, T. et al. Mastering the surface strain of platinum catalysts for efficient electrocatalysis. *Nature* **598**, 76–81 (2021).
49. Tsai, H. et al. Light-induced lattice expansion leads to high-efficiency perovskite solar cells. *Science* **360**, 67–70 (2018).
50. Seehra, M. S., Narang, V., Geddam, U. K. & Stefaniak, A. B. Correlation between X-ray diffraction and Raman spectra of 16 commercial graphene-based materials and their resulting classification. *Carbon* **111**, 380–385 (2017).
51. Gabhi, R. S., Kirk, D. W. & Jia, C. Q. Preliminary investigation of electrical conductivity of monolithic biochar. *Carbon* **116**, 435–442 (2017).
52. Jiang, Y. et al. Spontaneous deposition of uniformly distributed ruthenium nanoparticles on graphitic carbon nitride for quantifying electrochemically accumulated H<sub>2</sub>O<sub>2</sub>. *Chin. J. Chem.* **39**, 3369–3374 (2021).
53. Xu, Y. et al. Nickel nanoparticles encapsulated in few-layer nitrogen-doped graphene derived from metal-organic frameworks as efficient bifunctional electrocatalysts for overall water splitting. *Adv. Mater.* **29**, 1605957 (2017).
54. Zhuang, Y., Han, S., Fang, Y., Huang, H. & Wu, J. Multidimensional transitional metal-actuated nanoplatforms for cancer chemodynamic modulation. *Coord. Chem. Rev.* **455**, 214360 (2022).
55. Lu, X. et al. Bioinspired copper single-atom catalysts for tumor parallel catalytic therapy. *Adv. Mater.* **32**, 2002246 (2020).
56. Huo, M., Wang, L., Wang, Y., Chen, Y. & Shi, J. Nanocatalytic tumor therapy by single-atom catalysts. *ACS Nano* **13**, 2643–2653 (2019).
57. Singh, N. & Muges, G. CeVO<sub>4</sub> nanozymes catalyze the reduction of dioxygen to water without releasing partially reduced oxygen species. *Angew. Chem. Int. Ed.* **58**, 7797–7801 (2019).
58. Wei, C. et al. Iridium/ruthenium nanozyme reactors with cascade catalytic ability for synergistic oxidation therapy and starvation therapy in the treatment of breast cancer. *Biomaterials* **238**, 119848 (2020).
59. Chen, X. et al. Chiral ruthenium nanozymes with self-cascade reaction driven the NO generation induced macrophage M1 polarization realizing the lung cancer “cocktail therapy”. *Small* **19**, 2207823 (2023).

## Acknowledgements

The work was supported by the National Nature Science Foundation (No. 82072065, L.L.), the Strategic Priority Research Program of the Chinese Academy of Sciences (No. XDA16021103, L.L.), the Fundamental Research Funds for the Central Universities (E2EG6802X2, L.L.), and the National Youth Talent Support Program (L.L.).

## Author contributions

S.Z., L.L. conceived the idea and designed the project. S.Z., Z.Z., Q.Z., Z.Y., G.C., J.W. and C.X. performed the experiments and analyzed the results. S.Z. and L.L. assisted with the figure production and experiment design. S.Z. and L.L. wrote and revised the original draft of the manuscript. L.L. supervised the whole project. All authors discussed the results and commented on the manuscript.

## Competing interests

The authors declare no competing interests.

## Additional information

**Supplementary information** The online version contains supplementary material available at <https://doi.org/10.1038/s41467-024-52277-7>.

**Correspondence** and requests for materials should be addressed to Linlin Li.

**Peer review information** *Nature Communications* thanks Zhenxing Li, Yongquan Qu and the other, anonymous, reviewer(s) for their contribution to the peer review of this work. A peer review file is available.

**Reprints and permissions information** is available at <http://www.nature.com/reprints>

**Publisher's note** Springer Nature remains neutral with regard to jurisdictional claims in published maps and institutional affiliations.

**Open Access** This article is licensed under a Creative Commons Attribution-NonCommercial-NoDerivatives 4.0 International License, which permits any non-commercial use, sharing, distribution and reproduction in any medium or format, as long as you give appropriate credit to the original author(s) and the source, provide a link to the Creative Commons licence, and indicate if you modified the licensed material. You do not have permission under this licence to share adapted material derived from this article or parts of it. The images or other third party material in this article are included in the article's Creative Commons licence, unless indicated otherwise in a credit line to the material. If material is not included in the article's Creative Commons licence and your intended use is not permitted by statutory regulation or exceeds the permitted use, you will need to obtain permission directly from the copyright holder. To view a copy of this licence, visit <http://creativecommons.org/licenses/by-nc-nd/4.0/>.

© The Author(s) 2024